Intrinsic magnetic properties and microstructural characteristics of FePt thin films with segregated rare earth elements prepared by a combinatorial high-throughput sputtering system

D. Ogawa,[1, a)] Y. Iwasaki,[2] J. Uzuhashi,[1] Y. Sasaki,[1] M. Kotsugi,[3] and Y. K. Takahashi[1, a)]
[1)]*National Institute for Materials Science, Tsukuba 305-0047, Japan*
[2)]*Center for Basic Research on Materials (CBRM), National Institute for Materials Science (NIMS), Tsukuba 305-0047, Japan*
[3)]*Department of Materials Science and Technology, Tokyo University of Science, Tokyo 125-8585, Japan*

(Dated: 9 July 2025)

This study undertakes comprehensive experimental validations based on theoretical predictions of the impact of Er and Tm doping on the magnetic properties of FePt thin films. Initial theoretical investigations indicate that doping with rare earth elements may result in promising alterations to the magnetic properties of the FePt thin films, with Er doping in particular offering a promising avenue for further study. Experimental synthesis via a combinatorial high-throughput sputtering system, which enables precise control over the composition of FePt thin films, achieves the desired magnetic properties. Small quantities of dopants, specifically 0.35 at.% Er, substantially enhance the key magnetic properties of saturation magnetization ($\mu_0 M_s$), anistropy constant (K_u) at room temperature, and the Curie temperature (T_C). Precise microstructural observations of a sample show that Er segregates at grain boundaries, voids, and the substrate/FePt interface, where Er preferentially replaces Fe sites. In other regions of the FePt grains, Er is not solid-soluble, and pure FePt and FePtEr form a composite material in the order of tens of nm. The incorporation of Er also influences the damping constant α. The findings of this study substantiate the intrinsic characteristics of Er-doped films, particularly the enhanced $\mu_0 M_s$, K_u and T_C attainable with nominal dopant concentrations, and facilitate the realization of ultimate magnetic recording densities anticipated for future data storage technologies.

Keywords: heat-assisted magnetic recording, FePt, combinatorial, high throughput, machine learning, rare-earth doping, intrinsic magnetic properties, microstructure, damping constant

I. INTRODUCTION

Heat-assisted magnetic recording (HAMR)[1,2] has emerged as a pivotal technology in the evolving landscape of high-density data storage, particularly in the era of big data. This technology offers a promising alternative to traditional recording methods by potentially exceeding areal densities of 4 Tb/in^2, considering the anisotropy constant of 7 MJ/m^3 and saturation magnetization of 1.4 T for FePt grains[3]. However, the transition of HAMR technology from 1 Tb/in^2 to 4 Tb/in^2 involves several significant challenges. These challenges include reducing the size of magnetic grains, enhancing thermal gradients, improving magnetic anisotropy, and reducing noise. Addressing these challenges requires complex solutions that are supported by comprehensive research and innovation in the fields of materials science and magnetic recording technologies. A significant challenge lies in reducing the magnetic grain size to increase the areal density while maintaining the thermal stability and signal-to-noise ratio (SNR). The proposed media specifications for advancing towards from 2 to 4 Tb/in^2 include reducing the center-to-center grain distance (D_p) from 7.0 nm to approximately 5.1 nm and the magnetic core size (D_{core}) from 6.0 nm to 4.3 nm. The variability in the grain diameter (σ/mean grain diameter) should be finely controlled within a range of 10-15%, ensuring uniformity in size across the media[4]. Furthermore, a film thickness (t) of 8.2 nm is necessary to guarantee a sufficient SNR. This implies that a highly severe microstructure is required, specifically, an aggregate structure (columnar structure) of FePt core grains with an aspect ratio (t/D) of 1.60[4]. Recently, h-BN has been extensively studied as a promising material to satisfy these requirements[5–8]. In addition to the microstructure control, another approach to maintain the SNR while achieving 4Tb/in^2 is to increase the $\mu_0 M_s$ of the FePt core grains. By increasing the $\mu_0 M_s$ of the FePt grains, the film thickness for maintaining the SNR can be reduced, which is expected to relax the above aspect ratio requirement and simplify achieving a higher density. It has been reported that the addition of Nd increases the spin and orbital moment of Fe, with a high orbital moment of Nd and an increase in $\mu_0 M_s$[9]. The addition of Gd, and Tb[10,11] is of interest not only for HAMR applications but also for so-called all-optical switching (AOS), where non-collinear antiferromagnetic coupling with Fe is reported to lower $\mu_0 M_s$. However, the mechanism by which these additive elements alter the intrinsic magnetic properties has not yet been explained. The latest developments in first-principles calculations have demonstrated that the magnetocrystalline anisotropy energy (ΔE) of FePt is predominantly attributable to the robust spin-orbit coupling derived from heavy elements, such as Pt[12]. Despite the inability to explain the temperature dependence using the general $K(T)/M(T)^3$ relationship, first-principles approaches have been developed to elucidate the behavior at finite temperatures by incorporating trans-spin fluctuations[13]. Furthermore, hard X-ray photoelectron spec-

[a)]Corresponding author

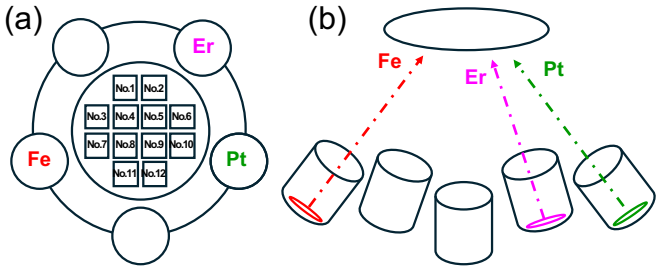

FIG. 1. (a) Target configuration and substrate location in the sputtering chamber. (b) Schematic of the cathode and substrate from the side.

troscopy (HAXPES) has revealed that in $L1_0$-ordered FePt thin films, the Pt 5d orbitals exert a significant influence on the perpendicular magnetic anisotropy (PMA) owing their robust hybridization with the Fe 3d state[14]. Thus, the origin of the intrinsic magnetic properties of $L1_0$-FePt is gradually being understood; however, much remains unknown. Therefore, this study will focuses on the improvement and evaluation of the intrinsic magnetic properties ($\mu_0 M_s$, K_u, and T_C) when additive elements are added to the FePt core grains, exploring materials that increase $\mu_0 M_s$ while maintaining K_u by adding a third element to the FePt grains. First-principles calculations are highly effective tools for the mechanistic elucidation of material properties but they are also useful in material exploration. Machine learning has recently emerged as a valuable tool for material exploration. By incorporating machine learning into first-principles data for prediction, the possibility of exploring optimal compositions in a wide composition space, such as the addition of two or more elements, that cannot be followed only by first-principles calculations, has been proposed[15,16]. This study initially concentrates on the elements Er, and Tm, which have been predicted to enhance $\mu_0 M_s$ through first-principles calculations[?] . The damping constant α is also a crucial parameter because high magnetic damping is preferred to achieve a higher SNR[17], and faster writing times[18]. In particular, the temperature dependence of α and its behavior near T_C are important for the practical applications of HAMR[19–22], and attempts have been made to understand these properties from experimental[23] and theoretical[24] perspectives.

In this study, the effects of Er and Tm doping on FePt thin films, which has been predicted to increase $\mu_0 M_s$ by first-principles calculations and has not been previously reported. To ensure efficient data collection, samples are prepared by using a combinatorial high-throughput sputtering system, in which multiple film compositions are obtained in a single deposition process. The first aim of this study is to comprehensively investigate the compositional dependence of the intrinsic magnetic properties of FePt thin films, such as $\mu_0 M_s$, K_u, T_C. The second aim is to investigate the microstructure and damping constant α in detail, focusing on compositions that showed improve the magnetic properties.

II. EXPERIMENTAL DETAILS

The films were deposited using a combinatorial high-throughput sputtering system, with an FePt-Er layer of approximately 30-40 nm deposited on a single-crystal MgO(001) substrate, which is well known to promote *c*-axis orientation and $L1_0$ ordering of FePt[25,26]. A 5 nm carbon cap was applied to all films to prevent oxidation. The substrate temperature and argon gas pressure employed during the deposition of FePt-Er were 500 °C and 10 mTorr, respectively. In the Fe, Pt, and Er target arrangements shown in Fig. 1, sputter discharges were performed at the sputter power and deposition time indicated in the Supplementary Material. The target diameter was ϕ 76.2 mm. The distance between the target and the substrate was 250 mm, and the angle of incidence was 45 °. For the sputtering of Er or Tm, the rate was controlled by placing a masking plate directly over the target to suppress the excessively high rates. A combinatorial method was employed to fabricate films with multiple compositions using a single deposition process. This involved the placement of 10 mm square MgO(001) substrates in the configuration shown in Fig. 1(a) on the substrate holder, with no rotation of the substrates during deposition. The concept of employing a combinatorial approach by using a thin film process has a substantial history[27–29] and has recently demonstrated considerable potential as a highly effective tool for the acquisition of large datasets in conjunction with machine learning[30,31].

Magnetization curves were analyzed utilizing a vibrating sample magnetometer (VSM) using TM-VSM211483ASE (*Tamagawa*) and a superconducting quantum interference device (SQUID) using MPMS3 (*Quantum Design*). The in-plane (IP) hysteresis loops were measured using a Dynacool (*Quantum Design*) with a 14 T maximum magnetic field, which was equipped with a large bore coil set. The uniaxial anisotropy constant K_u was estimated by anomalous hole effect (AHE) torque measurements using a Dynacool (*Quantum Design*) with 9 T maximum magnetic field, which was equipped with a standard manufacturer's rotator and resistance measurement options. Further details regarding the AHE torque measurements and analyses can be found in the relevant literature[32,33]. The temperature dependence of magnetization was measured using a SQUID-VSM (*Quantum Design*). The Curie temperatures (T_c) were determined by fitting *M*-*T* curves using the Kuz'min formula[34].

Regression analysis with using the random forest[35] model was performed using the software WAVEBASE[36] (*Toyota Motor Corporation*) to complementarily predict the $\mu_0 M_s$ between the gaps in the experimental data points for compositions (x,y) in the $(Fe_{50-x}Pt_x)_{100-y}$-Er_y (X=Er,Tm) system, based on the experimental data gathered by the combinatorial method.

For the analysis of the crystal structures, X-ray diffraction (XRD) profiles were obtained, and the $L1_0$ ordering parameter, *S* and lattice parameters were evaluated using a Smartlab (*Rigaku*). The method employed for estimating *S* was in accordance with that described in previous literature[37–39]. The film thicknesses of all samples were estimated by X-ray reflectivity (XRR) measurements and fitting the obtained data.

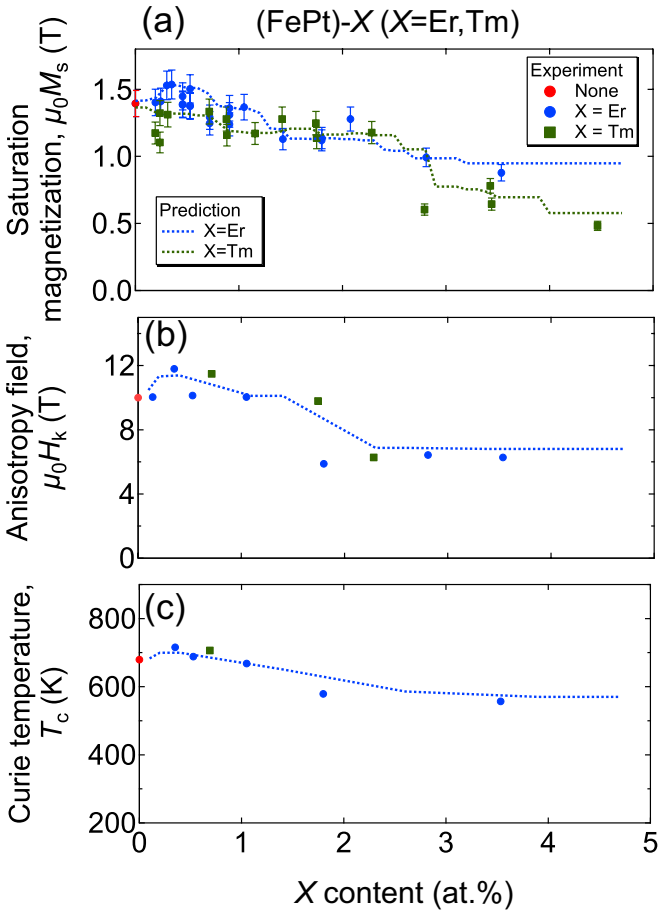

FIG. 2. X (X=Er,Tm) content dependence of the (a) saturation magnetization $\mu_0 M_s$, (b) anisotropic field $\mu_0 H_k$, and (c) Curie temperature T_C for FePt-X thin films. Dotted lines are predicted values when the Er was substituted at the Fe site in $Fe_{50-x}Pt_{50}Er_x$ by regression analysis.

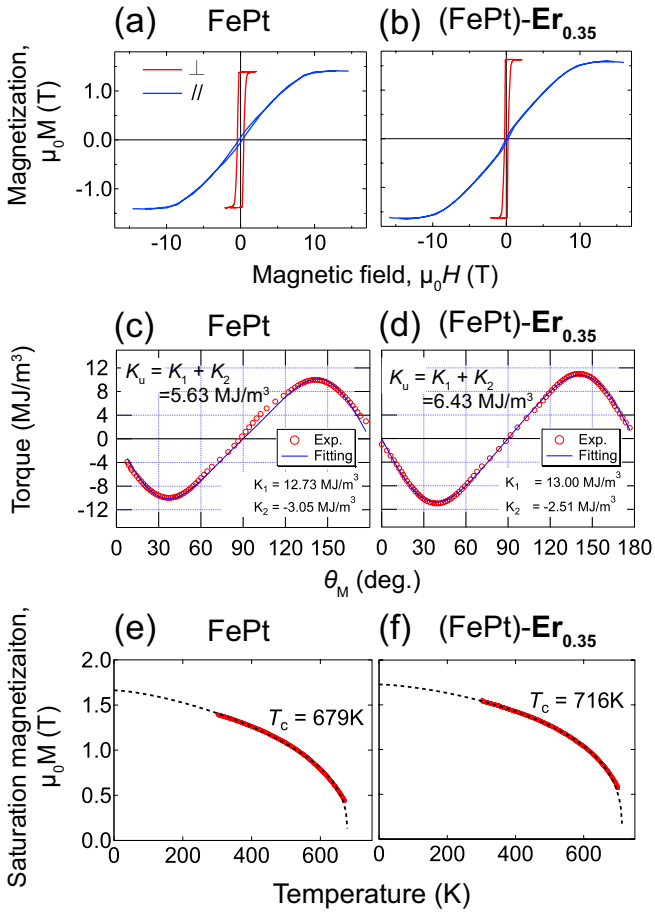

FIG. 3. (a) Magnetization curves in the out-of-plane (⊥) and in-plane (//) directions at 300 K for (a) FePt thin film without Er addition and (b) FePt thin film with 0.35 at.% Er addition. AHE torque and fitting curves at 300 K for (c) FePt thin film without Er addition and (d) FePt thin film with 0.35 at.% Er addition. M-T curve for for (e) FePt thin film without Er addition and (f) FePt thin film with 0.35 at.% Er addition. Black dashed lines are Kuz'min fitting functions.

The compositional analysis was conducted using X-ray fluorescence (XRF) spectroscopy, with a ZSX Primus II system (*Rigaku*).

The plane view and cross-sectional scanning transmission electron microscopy (STEM) observations with energy-dispersive X-ray spectroscopy (EDS) were performed using a Spectra Ultra S/TEM (*Thermo Fisher Scientific*). Plane view TEM lamellae were prepared by chemical etching, and cross-sectional TEM lamellae and needle-shaped specimens for atom probe tomography (APT) were fabricated using a focused ion beam (FIB) with a scanning electron microscopy (SEM) dual-beam system Helios5UX (*Thermo Fisher Scientific*). APT measurements were carried out using LEAP5000XS (*CAMECA*) in the 355 nm UV laser pulsing mode with 30 pJ energy at a specimen temperature of 30 K. Data were visualized and analyzed using the APsuite 6.1 program (*CAMECA*).

The damping constant was evaluated by using the all-optical time-resolved magneto-optical Kerr effect (AO-TRMOKE). The laser pulse source was a Yb:KGW laser system with a wavelength, pulse width, and pulse repetition rate of 1028 nm, 290 fs, and 10 kHz, respectively. The wavelength of the probe laser pulse was converted to 514 nm by using a BaB_2O_4 (BBO) crystal. The pump beam amplitude was modulated using a mechanical chopper with a modulation frequency of 870 Hz. The pump induced change in the Kerr rotation angle of the reflected probe laser pulse that was detected using a balanced photodiode detector and lock-in amplifier by varying the optical delay Δt between the pump and probe laser pulse with a delay line. The laser spot size for the pump and probe laser beam were 126 and 63 μm in diameter, respectively. The pump fluence was fixed to be 2.4 mJ/cm^2 and the probe fluence was below 0.5 mJ/cm^2. A magnetic field of 7 T was applied at 80 ° with respect to the film normal during the TRMOKE measurements[40].

III. RESUSTS AND DISCUSSION:

A. Magnetic Properties

Fig. 2 illustrates the (a) saturation magnetization ($\mu_0 M_s$) at 300 K, (b) anisotropy field ($\mu_0 H_k$) at 300 K, and (c) Curie temperature of the FePt-X films (X=Er, Tm) as a function of the Er and Tm atomic contents. When the configuration of the cathodes in Fig. 1 was used, the Er and Tm contents and the Fe and Pt composition ratios change naturally. $L1_0$-FePt varies in $\mu_0 M_s$ and K_u as the ratio of Fe to Pt changes, with the composition of x = 50 ~60 in Fe_xPt_{100-x} having the largest value[41–43]. Consequently, a regression analysis utilizing the composition (x, y) as a descriptor and $\mu_0 M_s$ as the target variable was used to predict $\mu_0 M_s$ when the atomic ratio percentage of Pt was assumed to be 50%. The blue and green dotted lines in Fig. 2(a) correspond to the predicted values of $\mu_0 M_s$ assuming that the atomic percentage of Pt is 50% in the Er- and Tm-doped samples was 50%, respectively. As a result, an increase in $\mu_0 M_s$ was observed with very small additions of Er $\leq$ 0.5 at.%. In the composition region of Er $\geq$ 1 at.%, $\mu_0 M_s$ decreased monotonically. In contrast, the $\mu_0 M_s$ value decreased linearly with an increasing Tm content across all composition ranges, exhibiting no $\mu_0 M_s$ peaks, as seen in the Er-doped samples. It was observed that the $\mu_0 H_k$ and T_C increased in the region of a very low composition, $\leq$ 1 at.% for both Er- and Tm-doped samples. Increases in $\mu_0 M_s$, K_u and T_C were observed with the addition of a very small amount of Er (0.35 at%). Therefore, focusing on this composition, Fig. 3 shows: (a) the magnetization curves with an induced external field along the out of plane ($\perp$) and in-plane (//) directions at 300 K with and without an Er-doped sample, (b) the magnetic torque measurement and fitting results using AHE at 300 K, and (c) the M-T curves. Fig. 3(a) shows that $\mu_0 M_s$ was 1.39 T at 300 K without the addition of Er, whereas it increased to 1.54 T with the addition of 0.35 at% Er. $\mu_0 H_k$ also increased from 10.0 T to 11.8 T with the addition of Er. Fig. 3(b) shows that the anisotropy constant K_u (K_1+K_2) also increased from 5.63 MJ/m^3 without Er addition to 6.43 MJ/m^3 with a very small Er addition of 0.35 at%. From Fig. 3(c), the Curie temperature increased from 679 K to 716 K with the addition of Er. However, no difference in $\mu_0 M_s$ was observed between the two samples at temperatures close to 0 K. Therefore, the increase in $\mu_0 M_s$ and K_u at 300 K owing to the addition of 0.35 at.% Er can be attributed mainly to the increase in the Curie temperature, which reduced the rate of decrease with temperature. The $L1_0$ ordering parameter S, estimated from XRD, was 0.956 and 0.926 for samples with and without 0.35 at.% Er, respectively. The observation that there is minimal alteration in the $L1_0$ ordering parameter S with the incorporation of Er indicates that the observed changes in the magnetic properties are a consequence of an intrinsic modification of the magnetic properties of the FePt grains. The detailed information concerning the composition, thickness, lattice constant c, $L1_0$ order parameter, $\mu_0 M_s$, T_C, and $\mu_0 H_k$ of two samples shown in Fig. 3 is listed in Table I, and all the samples described in this paper is listed in Table S1 of the supplemental material.

TABLE I. Lattice constants a, c, $L1_0$ ordering parameter, and magnetic properties of FePt thin films without Er addition and with Er 0.35 at.% addition.

		without Er	Er 0.35 at.%
Lattice constants	a (nm)	0.387	0.387
	c (nm)	0.372	0.371
$L1_0$ order parameter		0.926	0.956
M_s (T)	50 K	1.64	1.66
	300 K	1.39	1.54
K_u (MJ/m^3)	50 K	8.00	7.34
	300 K	5.63	6.43
H_k (T)	300 K	10.0	11.8
T_C (K)		679	716

B. Microstructure Analysis

Evaluation of the magnetic properties revealed that the sample with an addition of 0.35 at.% Er exhibited the most significant improvement. Therefore, microstructure observations were conducted for this sample. Fig. 4 shows a cross-sectional high-angle annular dark-field (HAADF)-STEM image of a sample with 0.35 at.% Er incorporated. As shown in Fig. 4(a), the image reveals the formation of a continuous film of a FePt-Er film on the MgO substrate. However, an examination of the upper portion of the film revealed the formation of valleys in certain areas, despite its continuous nature. Fig. 4(b)-(d) show the magnified HAADF-STEM image and EDS elemental maps of FePt and Er, respectively. The white arrows in Fig. 4(c) and (d) indicate the locations of the valleys. In Fig. 4(d), pink arrows indicate Er segregation. Small voids were formed just below the valleys Er was preferentially segregated near these voids. EDS maps of FePt and Er in different regions are shown in Fig. 4(e). The EDS line profile of white area in Fig. 4(e) is shown in Fig. 4(f). The results showed that Fe, Pt and Er were uniformly distributed; however, 1.0 at.% of Er tended to be segregated near the interface between the MgO substrate and the FePt layer. Fig. 4(g)-(i) show the HAADF-STEM image focused on near the valley, and EDS maps of FePt and Er. The dark-contrast region in Fig. 4(g) corresponds to a void. A comparison with the Er distribution in Fig. 4(i) revealed that Er was preferentially segregated around the void. Fig. 5 shows the 3D atom maps for 0.35at% Er-doped FePt-Er film. The detection limit of EDS is typically approximately 1 at.%; however, APT has a significantly higher chemical sensitivity[44]. Although dependent on the target materials and analysis conditions, 0.002at% of Mg dopant in GaN was successfully measured using APT[45]. Fig. 5(a) shows Fe, Pt, Mg, and O atoms displayed as red, green, purple, and blue dots, respectively. In contrast, Fig. 5(b) shows the Er atoms as pink dots. The preferentially segregated Er at the interface between the MgO substrate and the FePt layer can also be seen here. In addition, Er was preferentially present in the upper regions of the FePt layer. Fig. 5(c) shows the 3D atom probe analysis region selected in the blue frame of Fig. 5(b) from the top. As indicated by the cross-sectional image in Fig. 4, Er was segregated along grain boundaries and voids in a network-like pattern. From the mass spectrum in Fig. 5(d), the Pt+++ peak,

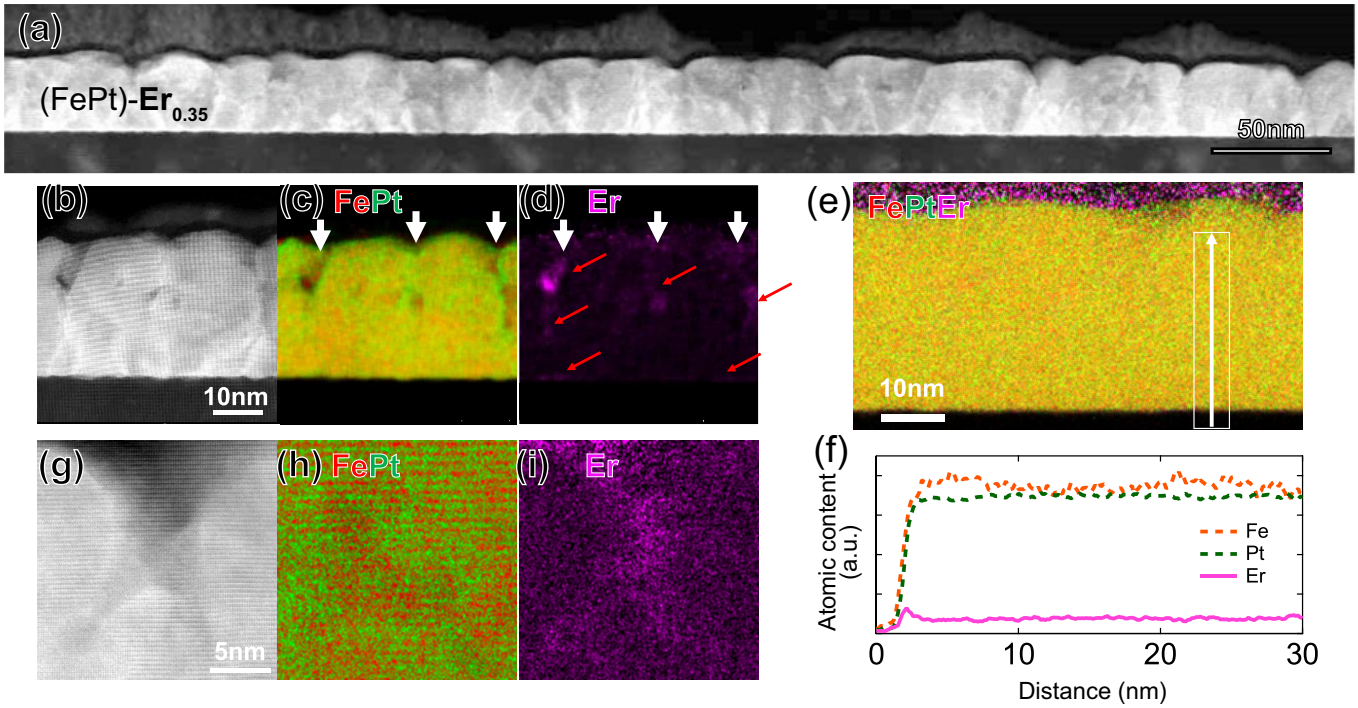

FIG. 4. (a) Low-magnification cross-sectional HAADF-STEM image of FePt-Er thin film with 0.35 at.% Er addition, (b) higher magnification HAADF-STEM image, (c) EDS elemental map of FePt corresponding to the field of view in (b), (d) EDS elemental map of Er corresponding to the field of view in (b), (e) EDS elemental map of FePtEr for another area and EDS line profile of FePtEr in the white frame, (f) EDS line profile in the white region shown in (e), (g) HAADF-STEM image focusing on the valley, (h) EDS elemental map of FePt corresponding to the region in (g), and (i) EDS elemental map of Er corresponding to the region in (g).

Er+++ and Er++ peaks were identified, suggesting that Er was indeed present, at least as a divalent or trivalent ion. However, no peaks attributable to Er were observed from the mass spectrum of the region excluding Er segregation at the grain boundaries, near voids, and at the FePt/MgO interface. This finding demonstrates that Er was not uniformly solid-soluble in the FePt grains. Fig. 5(c) shows that pure FePt and FePt-Er are intermingled to a depth of approximately tens of nm. Mass spectrum analysis demonstrated that the Er content in the region where Er was present was approximately 1 at.%. Fig. 6 illustrates the results of the top-view HAADF-STEM observations conducted on a sample containing 0.35 at.% Er. Fig. 6(a)-(c) show the HAADF-STEM image, and FePt and Er EDS elemental maps, respectively. Fig. 6(d) shows the EDS line profiles of Fe, Pt, and Er in the areas in Fig. 6(c). The upper and lower graphs illustrate the intensity and atomic content of each element, respectively. The dark-imaged area in Fig. 6(a) was confirmed to be a void based on the reduced intensity observed in Fig. 6(d). Near this void, there was an increase in the atomic content of Er and a corresponding decrease in the atomic concentration of Fe. The Er atoms were segregated preferentially in the region near the void, and the Fe sites were preferentially substituted by Er in that region. Fig. 6(e) shows a HAADF-STEM image of a separate area of the sample with 0.35 at.% Er added. Fig. 6(h) shows the line profiles of Fe, Pt, and Er in the white region of Fig. 6(g) in the same format in Fig. 6(d). The black dotted lines in Fig. 6(e) indicate the grain boundaries. Fig. 6(g) shows that Er was also segregated near the vicinity of the grain boundary. The magnified sections of the atomic resolution on the left and right serve to highlight the areas in Fig. 6(e) where Er was present and absent, respectively. A comparison of these highlighted areas shows that at least the same periodic fct structure was maintained in the regions with and without Er. It was not possible to ascertain from this image whether the degree of $L1_0$ ordering was preserved in these areas. However, the overall $L1_0$ order of the sample, as estimated from the XRD results, showed minimal variation with or without Er. This indicates that the $L1_0$ structure was maintained even in regions where Er was segregated. It was determined that Er was not uniformly solid-soluble in the FePt grains. Additionally, it was observed that $L1_0$-FePtEr was preferentially segregated around the void/grain boundaries and the MgO/FePt interface, with a size of approximately tens of nm. Generally, examples of nanoscale void formation and segregants around voids by doping additives are common and have been reported in other material systems. For example, it has been reported that doping Sb into p-type ZnO nanowires may improve p-type properties owing to the formation of nanoscale voids as the Sb segregates around voids during the growth process, and the surrounding ZnO grows more slowly than normal[46]. In a $CoSi_2$ sample, the formation of voids at the interface by BF_2 doping contributes to increased sheet resistance and thermal stability, and is expected to be used in ultra large scale integration (ULSI) devices[47]. In these cases, the formation of voids and segregants around voids has a positive effect on improv-

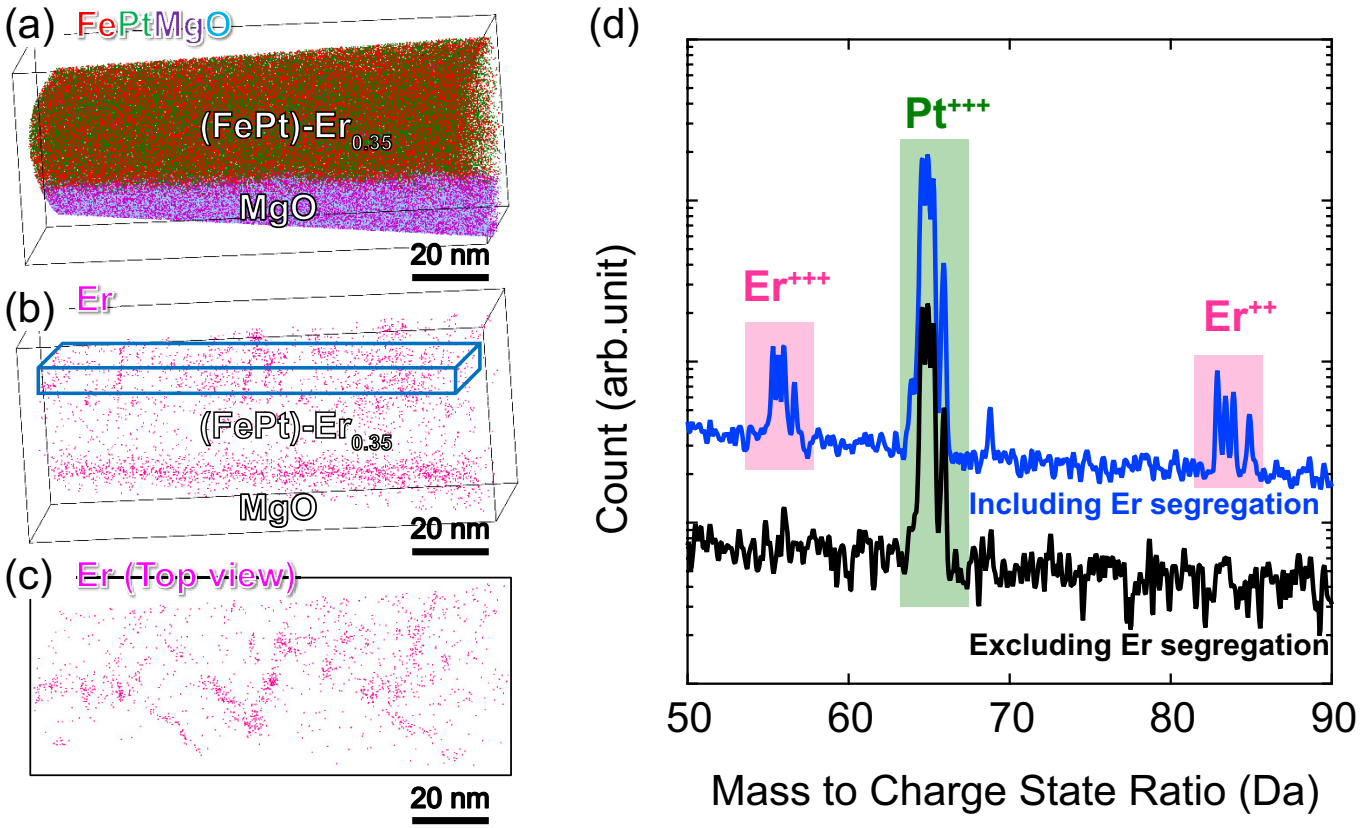

FIG. 5. 3D atom probe tomography reconstruction for 0.35 at.% Er-doped FePt-Er film. (a) Fe, Pt, Mg, and O atoms displayed as red, green, purple, and blue dots, respectively; (b) Er atoms displayed as pink dots; (c) Er atoms displayed as pink dots from the top view; (d) Mass spectrum from the entire FePt-Er film including Er segregation displayed as a blue line and the region excluding Er segregation at grain boundaries and the FePt/MgO interface displayed as a black line.

ing properties, and it may not be necessary to suppress them. However, void formation can generally be controlled by optimizing the amount of additives and the heat treatment process. As the heat-treatment temperature was fixed at 500 °C in this study, further improvements may be required. This is an issue for future research.

Regarding the magnetic properties of the FePt-Er films, it can be surmised that at 300 K, the $\mu_0 M_s$ and K_u values of pure $L1_0$-FePt grains and $L1_0$-FePtEr near voids/grain boundaries and the MgO/FePt interface should differ. Despite the presence of disparate M_s and K_u values, the single-phase behavior observed in the magnetization curves of the Er-doped samples depicted in Fig. 3(b) may be attributed to the exchange coupling between the two phases. In composites with two $\mu_0 M_s$ and K_u values, the magnetization curve behaves in a single-phase manner, and the $\mu_0 M_s$ and K_u are averaged out; if the exchange coupling between the two phases is sufficiently active, is experimentally real[48,49] and theoretically explained[50]. Therefore, it is possible that the averaged $\mu_0 M_s$ and K_u of $L1_0$-FePt and $L1_0$-FePtEr may be present in Fig. 3, whereas $\mu_0 M_s$ and K_u in the $L1_0$-FePtEr single-phase are expected to be larger than those in Fig. 3. To evaluate the intrinsic magnetic properties, a continuous film sample was analyzed. Microstructural analysis of this film showed that Er was preferentially segregated around the void/grain boundaries and MgO/FePt interface.

C. Dynamics

Finally, in order to ascertain the damping constant of a sample with 0.35 at.% Er, TRMOKE measurements were conducted. Figs.7(a) and 7(b) show the TRMOKE data in the time- and frequency-domains,respectively, measured at room temperature. Time-domain data were analyzed using the least squares method through the following equation, as shown by the red curves in Fig. 7(a):

$$\Delta\varphi_K = A_0 + A_1 \exp(-\nu \cdot \Delta t) + B_0 \exp\left(-\frac{\Delta t}{\tau}\right) \sin(2\pi f \cdot \Delta t + \delta_0), \quad (1)$$

The first and second terms are background signals, with an offset A_0, intensity of magnetization recovery process A_1, and its recovery rate ν. The third term with a precession amplitude B_0, decay time τ, frequency f, and initial phase δ_0 describes the magnetization precessional motion. The effective damping constant α_{eff} can be evaluated using $\alpha_{\text{eff}} = \frac{1}{2}\pi f \tau$. The pre-

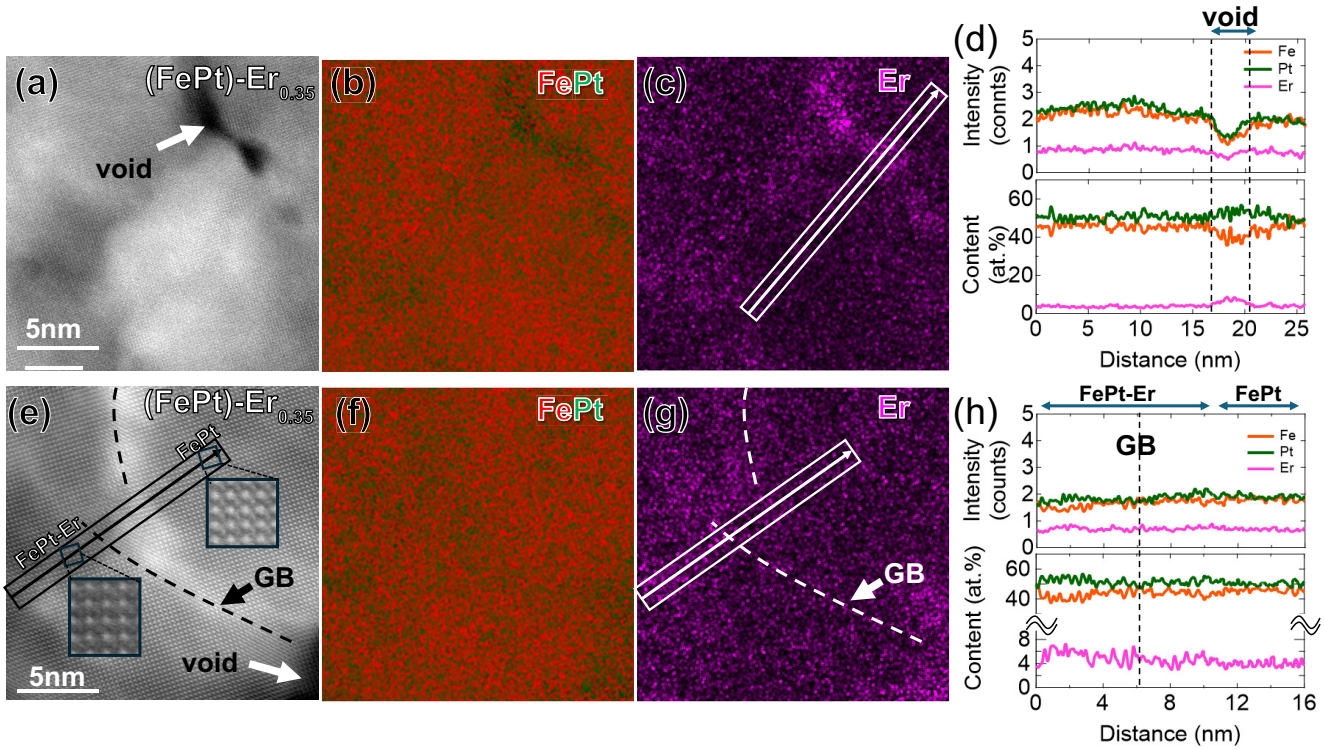

FIG. 6. (a) HAADF-STEM image of FePt-Er film with 0.35 at.% Er added, observed from the top view; (b) EDS elemental map of FePt in the field of view of (a); (c) EDS elemental map of Er; (d) EDS line profiles of Fe, Pt, and Er corresponding to the white area in (c), where the upper and lower graphs correspond to the intensity and atomic concentration, respectively; (e) HAADF-STEM image observed from the top view in another area, (f) EDS elemental map of FePt in the field of view of (e); (g) EDS elemental map of Er; (h) EDS line profiles of Fe, Pt, and Er corresponding to the white area in (g), where the upper and lower graphs correspond to the intensity and atomic concentration, respectively.

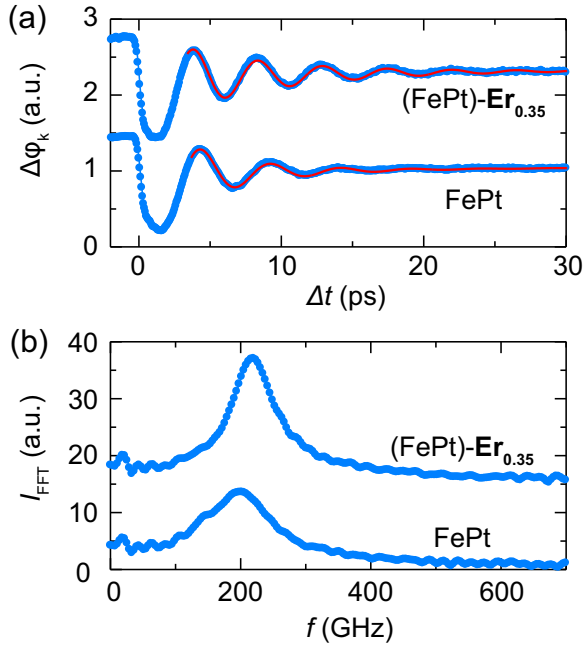

FIG. 7. (a) Time-domain TRMOKE data, (b) frequency-domain data for FePt thin films without Er and with a 0.35 at.% Er addition.

cession frequency increased from $f = 203$ GHz to 220 GHz by introducing 0.35 at.% of Er for the FePt film, which is consistent with the increase of perpendicular magnetic anisotropy.

The α_{eff} for the FePt film without Er was estimated to be 0.17 which is nearly equal to a FePt continuous film with large extrinsic contributions owing to the two-magnon scattering and PMA distribution in the film measured at 300 K[23]. However, the α_{eff} for the FePt film with 0.35 at.% Er was decreased to 0.10. In General, Gilbert damping constants arise from electronic transitions due to spin-orbit interactions[51,52]. Er belongs to the heavy rare earth group, which contains a substantial number of electrons in the f-orbital. Consequently, the spin-orbit interaction should be considerable. There have been experimental instances where the damping constant has been observed to increase with the addition of rare earth elements[53–55].

However, due to the large extrinsic contributions to the α_{eff}, it is difficult to discuss the intrinsic damping modification owing to the electrons in the f-orbital. Therefore, it was considered that the decrease in α_{eff} by Er-doping may be attributed to extrinsic contributions modified by microstructural alterations, and magnetic di-polar and exchange coupling changes. Further detailed investigations are required to separate the external factors from the intrinsic Gilbert damping constant α by measuring the angular dependence of the applied magnetic

field.

IV. CONCLUSION

FePt-X (X = Er, Tm) films were deposited using a combinatorial high-throughput method. This method wass demonstrated to facilitate a comprehensive investigation of the dependence of $\mu_0 M_s$, $\mu_0 H_k$ and T_C on the concentration of X. These findings indicate that the doping with a small amount of Er (0.35 at.%) enhanced $\mu_0 M_s$ at 300 K from 1.39 T to 1.54 T, the K_u at 300 K from 5.63 MJ/m^3 to 6.43 MJ/m^3, and the T_C from 679 K to 716 K. TEM observations and 3D atom probe analysis demonstrated that Er was segregated at approximately 1 at.% around voids, grain boundaries, and near the MgO substrate/FePt interface. It was assumed that Er was not solidl-soluble in the FePt grains and that the $L1_0$-FePt grains and $L1_0$-FePtEr were mixed in a complex manner on the order of tens of nm. The EDS line profiles from the top-view TEM images showed that Er preferentially replaced the Fe sites. Furthermore, Er-doping of FePt films had a significant effect on the damping constant.

In this study, the intrinsic magnetic properties of a continuous film sample were ealuated. Based on microstructural analysis, it was found that Er was preferentially segregated around the void/grain boundaries and the MgO/FePt interface. For HAMR applications with an FePt granular structure, more interfaces should exist than in continuous films; therefore, it is expected that Er will exist preferentially and that granular films of FePt core material with improved $\mu_0 M_s$ can be produced, contributing to further density increases.

V. ACKNOWLEDGMENTS

The authors thank T. Hiroto, S. Nimori (NIMS) for their assistance with the use of the experiment machines. The authors also thank K. Suzuki (NIMS) for her contribution in conducting experiments. This work was supported in part by the Data Creation and Utilization-Type Material Research and Development Project "Digital Transformation Initiative Center for Magnetic Materials" (Grant No. JPMXP1122715503), the JST-CREST (Grant No.JPMJC22C3), MEXT program "Data Creation and Utilization-Type Material Research and Development Project" (Grant No. JPMXP1122715503), and JST-CREST (Grant No. JPMJCR21O1). A part of this work was supported by the Electron Microscopy Unit, National Institute for Materials Science (NIMS).

[1] J. J. M. Ruigrok, "Limits of conventional and thermally-assisted recording," J. Magn. Soc. Jpn. **25**, 313–321 (2001).

[2] M. Kryder, E. Gage, T. McDaniel, W. Challener, R. Rottmayer, G. Ju, Y.-T. Hsia, and M. Erden, "Heat Assisted Magnetic Recording," Proc IEEE Inst Electr Electron Eng **96**, 1810–1835 (2008).

[3] O. Ivanov, L. Solina, V. Demshina, and L. Magat, "Determination of the anisotropy constant and saturation magnetization, and magnetic properties of powders of an iron-platinum alloy," Phys. Met. Metallog. **35**, 81 (1973).

[4] D. Weller, G. Parker, O. Mosendz, E. Champion, B. Stipe, X. Wang, T. Klemmer, G. Ju, and A. Ajan, "A HAMR media technology roadmap to an areal density of 4 Tb/in^2," IEEE Trans. Magn. **50**, 1–8 (2014).

[5] C. Xu, B. Zhou, T. Du, B. S. D. C. S. Varaprasad, D. E. Laughlin, and J.-G. J. Zhu, "Understanding the growth of high-aspect-ratio grains in granular $L1_0$-fept thin-film magnetic media," APL Mater **10** (2022), 10.1063/5.0089009.

[6] C. Xu, B. S. D. C. S. Varaprasad, D. E. Laughlin, and J.-G. Zhu, "Fabrication of 16 nm Thick Granular $L1_0$ FePt-hBN Thin Film Media," IEEE Trans. Magn. **59**, 1–5 (2023).

[7] B. S. D. C. S. Varaprasad, C. Xu, M.-H. Huang, D. E. Laughlin, and J.-G. Zhu, "FePt–BN granular HAMR media with high grain aspect ratio and high $L1_0$ ordering on corning LotusTM NXT glass," AIP Adv **13** (2023), 10.1063/9.0000587.

[8] C. Xu, B. S. D. C. S. Varaprasad, D. E. Laughlin, and J.-G. Zhu, "Bias sputtering of granular $L1_0$-FePt films with hexagonal boron nitride grain boundaries," Sci. Rep **13** (2023), 10.1038/s41598-023-38106-9.

[9] D. B. Xu, C. J. Sun, J. S. Chen, S. M. Heald, B. Sanyal, R. A. Rosenberg, T. J. Zhou, and G. M. Chow, "Large enhancement of magnetic moment in $L1_0$ ordered FePt thin films by Nd substitutional doping," Journal of Physics D: Applied Physics **48**, 255001 (2015).

[10] N. Y. Schmidt, S. Abdulazhanov, J. Michalička, J. Hintermayr, O. Man, O. Caha, M. Urbánek, and M. Albrecht, "Effect of Gd addition on the structural and magnetic properties of $L1_0$-FePt alloy thin films," Journal of Applied Physics **132** (2022), 10.1063/5.0124652.

[11] N. Y. Schmidt, S. Laureti, F. Radu, H. Ryll, C. Luo, F. d'Acapito, S. Tripathi, E. Goering, D. Weller, and M. Albrecht, "Structural and magnetic properties of FePt-Tb alloy thin films," Physical Review B **100** (2019), 10.1103/physrevb.100.064428.

[12] Y. Kota and A. Sakuma, "Mechanism of Uniaxial Magnetocrystalline Anisotropy in Transition Metal Alloys," Journal of the Physical Society of Japan **83**, 034715 (2014).

[13] S. Yamashita and A. Sakuma, "First-Principles Study for Finite Temperature Magnetrocrystaline Anisotropy of $L1_0$ Type Ordered Alloys," Journal of the Physical Society of Japan **91** (2022), 10.7566/jpsj.91.093703.

[14] S. Ueda, M. Mizuguchi, Y. Miura, J. G. Kang, M. Shirai, and K. Takanashi, "Electronic structure and magnetic anisotropy of $L1_0$-fept thin film studied by hard x-ray photoemission spectroscopy and first-principles calculations," Applied Physics Letters **109** (2016), 10.1063/1.4959957.

[15] Y. Iwasaki, H. Jaekyun, Y. Sakuraba, M. Kotsugi, and Y. Igarashi, "Efficient autonomous material search method combining ab initio calculations, autoencoder, and multi-objective Bayesian optimization," Science and Technology of Advanced Materials: Methods **2**, 365–371 (2022).

[16] Y. Iwasaki, R. Toyama, T. Yamazaki, Y. Igarashi, M. Kotsugi, and Y. Sakuraba, "Autonomous search for half-metallic materials with B2 structure," Science and Technology of Advanced Materials: Methods **4** (2024), 10.1080/27660400.2024.2403966.

[17] N. A. Natekar, Z. Liu, S. Hernandez, and R. H. Victora, "SNR improvement by variation of recording and media parameters for a HAMR exchange coupled composite media," AIP Advances **8** (2018), 10.1063/1.5007072.

[18] R. Kikuchi, "On the Minimum of Magnetization Reversal Time," Journal of Applied Physics **27**, 1352–1357 (1956).

[19] N. A. Natekar, E. Roddick, and R. M. Brockie, "Interplay of the Thermal and Magnetic Fields in HAMR," IEEE Transactions on Magnetics **58**, 1–8 (2022).

[20] F. Akagi and N. Matsushima, "Relationship between temperature rise and thermal conductivity in a magnetic medium during heated dot magnetic recording," Japanese Journal of Applied Physics **62**, SB1001 (2022).

[21] R.-V. Ababei, M. O. A. Ellis, R. F. L. Evans, and R. W. Chantrell, "Anomalous damping dependence of the switching time in Fe/FePt bilayer recording media," Physical Review B **99** (2019), 10.1103/physrevb.99.024427.

[22] D. Richardson, S. Katz, J. Wang, Y. K. Takahashi, K. Srinivasan, A. Kalitsov, K. Hono, A. Ajan, and M. Wu, "Near-T_c ferromagnetic Resonance and Damping in FePt-Based Heat-Assisted Magnetic Recording Media," Physical Review Applied **10** (2018), 10.1103/physrevapplied.10.054046.

[23] Y. Sasaki, I. Suzuki, R. Mandal, S. Kasai, and Y. K. Takahashi, "Thermal Modulation of Magnetization Dynamics in Nanometer-Thick $L1_0$-FePt Nanogranular and Continuous Films for High-Density Magnetic Recording Media," ACS Appl. Nano Mater. **6**, 5901–5908 (2023).

[24] I. Kurniawan, Y. Miura, G. Xing, T. Tadano, and K. Hono, "Theoretical study of the effect of lattice dynamics on the damping constant of FePt at finite temperature," Phys. Rev. B **108**, 094426 (2023).

[25] B. M. Lairson and B. M. Clemens, "Enhanced magneto-optic Kerr rotation in epitaxial PtFe(001) and PtCo(001) thin films," Appl. Phys. Lett. **63**, 1438–1440 (1993).

[26] J.-U. Thiele, L. Folks, M. F. Toney, and D. K. Weller, "Perpendicular magnetic anisotropy and magnetic domain structure in sputtered epitaxial FePt (001) $L1_0$ films," J. Appl. Phys **84**, 5686–5692 (1998).

[27] K. Kennedy, T. Stefansky, G. Davy, V. F. Zackay, and E. R. Parker, "Rapid Method for Determining Ternary-Alloy Phase Diagrams," Journal of Applied Physics **36**, 3808–3810 (1965).

[28] N. Saunders and A. P. Miodownik, "Phase formation in co-deposited metallic alloy thin films," Journal of Materials Science **22**, 629–637 (1987).

[29] A. Ludwig, "Combinatorial fabrication of magnetic multilayer films," Applied Surface Science **223**, 78–83 (2004).

[30] Y. Hong, I. de Moraes, G. G. Eslava, S. Grenier, E. Bellet-Amalric, A. Dias, M. Bonfim, L. Ranno, T. Devillers, and N. M. Dempsey, "A high throughput study of both compositionally graded and homogeneous Fe–Pt thin films," Journal of Materials Research and Technology **18**, 1245–1255 (2022).

[31] A. Kovacs, J. Fischbacher, H. Oezelt, A. Kornell, Q. Ali, M. Gusenbauer, M. Yano, N. Sakuma, A. Kinoshita, T. Shoji, A. Kato, Y. Hong, S. Grenier, T. Devillers, N. M. Dempsey, T. Fukushima, H. Akai, N. Kawashima, T. Miyake, and T. Schrefl, "Physics-informed machine learning combining experiment and simulation for the design of neodymium-iron-boron permanent magnets with reduced critical-elements content," Frontiers in Materials **9** (2023), 10.3389/fmats.2022.1094055.

[32] T. Ono, N. Kikuchi, S. Okamoto, O. Kitakami, and T. Shimatsu, "Novel torque magnetometry for uniaxial anisotropy constants of thin films and its application to fept granular thin films," Applied Physics Express **11**, 033002 (2018).

[33] D. Ogawa, T. Yoshioka, X. Xu, Y. Takahashi, H. Tsuchiura, T. Ohkubo, S. Hirosawa, and K. Hono, "Magnetic anisotropy constants of $ThMn_{12}$-type $Sm(Fe_{1-x}Co_x)_{12}$ compounds and their temperature dependence," Journal of Magnetism and Magnetic Materials **497**, 165965 (2020).

[34] M. D. Kuz'min, "Shape of Temperature Dependence of Spontaneous Magnetization of Ferromagnets: Quantitative Analysis," Phys. Rev. Lett. **94**, 107204 (2005).

[35] L. Breiman, "Random Forests," Machine Learning **45**, 5–32 (2001).

[36] J. Wavebase (Toyota Motor Corporation), Tokyo, "[online] available: https://www.toyota.co.jp/wavebase/," (2022).

[37] C.-b. Rong, N. Poudyal, G. S. Chaubey, V. Nandwana, R. Skomski, Y. Q. Wu, M. J. Kramer, and J. P. Liu, "Structural phase transition and ferromagnetism in monodisperse 3 nm FePt particles," J. Appl. Phys. **102**, 043913 (2007).

[38] S. D. Granz and M. H. Kryder, "Granular $L1_0$ FePt (001) thin films for Heat Assisted Magnetic Recording," J. Magn. Magn. Mater. **324**, 287–294 (2012).

[39] E. Yang, D. E. Laughlin, and J.-G. Zhu, "Correction of Order Parameter Calculations for FePt Perpendicular Thin Films," IEEE Trans. Magn. **48**, 7–12 (2012).

[40] P. D. Bentley, Y. Sasaki, I. Suzuki, S. Isogami, Y. K. Takahashi, and H. Suto, "Development of $L1_0$-ordered FePt with low damping and large perpendicular magnetic anisotropy by engineering the nanostructure," Applied Physics Letters **126** (2025), 10.1063/5.0246369.

[41] C. M. Kuo, P. C. Kuo, H. C. Wu, Y. D. Yao, and C. H. Lin, "Magnetic hardening mechanism study in FePt thin films," Journal of Applied Physics **85**, 4886–4888 (1999).

[42] K. Barmak, J. Kim, L. H. Lewis, K. R. Coffey, M. F. Toney, A. J. Kellock, and J.-U. Thiele, "On the relationship of magnetocrystalline anisotropy and stoichiometry in epitaxial $L1_0$ CoPt (001) and FePt (001) thin films," Journal of Applied Physics **98** (2005), 10.1063/1.1991968.

[43] C. Y. You, Y. K. Takahashi, and K. Hono, "Magnetic properties and microstructures of Fe–Pt thin films sputter deposited under partial nitrogen gas flow," Journal of Applied Physics **98** (2005), 10.1063/1.1943509.

[44] B. Gault, M. P. Moody, J. M. Cairney, and S. P. Ringer, *Atom Probe Microscopy* (Springer New York, 2012).

[45] J. Uzuhashi, J. Chen, A. Kumar, W. Yi, T. Ohkubo, R. Tanaka, S. Takashima, M. Edo, K. Sierakowski, M. Bockowski, H. Sakurai, T. Kachi, T. Sekiguchi, and K. Hono, "Atomic-scale investigation of implanted Mg in GaN through ultra-high-pressure annealing," Journal of Applied Physics **131** (2022), 10.1063/5.0087248.

[46] K. C. Pradel, J. Uzuhashi, T. Takei, T. Ohkubo, K. Hono, and N. Fukata, "Investigation of nanoscale voids in Sb-doped p-type ZnO nanowires," Nanotechnology **29**, 335204 (2018).

[47] N.-S. Kim, H.-S. Cha, N.-K. Sung, H.-H. Ryu, K.-S. Youn, and W.-G. Lee, "Void formation during silicidation and its influence on the thermal stability of cobalt silicide," Journal of Vacuum Science amp; Technology A: Vacuum, Surfaces, and Films **20**, 1171–1176 (2002).

[48] R. Coehoorn, D. B. de Mooij, J. P. W. B. Duchateau, and K. H. J. Buschow, "NOVEL PERMANENT MAGNETIC MATERIALS MADE BY RAPID QUENCHING," Le Journal de Physique Colloques **49**, C8–669–C8–670 (1988).

[49] S. Hirosawa, H. Kanekiyo, T. Miyoshi, Y. Shigemoto, K. Murakami, Y. Senzaki, and T. Nishiuchi, "Development of high-coercivity nanocomposite permanent magnets based on $Nd_2Fe_{14}B$ and Fe_xB," Journal of Alloys and Compounds **408–412**, 260–265 (2006).

[50] E. Kneller and R. Hawig, "The exchange-spring magnet: a new material principle for permanent magnets," IEEE Transactions on Magnetics **27**, 3588–3560 (1991).

[51] K. Gilmore, Y. U. Idzerda, and M. D. Stiles, "Identification of the Dominant Precession-Damping Mechanism in Fe, Co, and Ni by First-Principles Calculations," Physical Review Letters **99** (2007), 10.1103/physrevlett.99.027204.

[52] V. Kamberský, "On the Landau–Lifshitz relaxation in ferromagnetic metals," Canadian Journal of Physics **48**, 2906–2911 (1970).

[53] A. Rebei and J. Hohlfeld, "Origin of Increase of Damping in Transition Metals with Rare-Earth-Metal Impurities," Physical Review Letters **97** (2006), 10.1103/physrevlett.97.117601.

[54] G. Woltersdorf, M. Kiessling, G. Meyer, J.-U. Thiele, and C. H. Back, "Damping by Slow Relaxing Rare Earth Impurities in $Ni_{80}Fe_{20}$," Physical Review Letters **102** (2009), 10.1103/physrevlett.102.257602.

[55] C. Luo, Z. Feng, Y. Fu, W. Zhang, P. K. J. Wong, Z. X. Kou, Y. Zhai, H. F. Ding, M. Farle, J. Du, and H. R. Zhai, "Enhancement of magnetization damping coefficient of permalloy thin films with dilute Nd dopants," Physical Review B **89** (2014), 10.1103/physrevb.89.184412.